

Advances in Geosciences
Vol. 21: Solar & Terrestrial Science (2008)
Ed. Marc Duldig
© World Scientific Publishing Company

**SOLAR MASS EJECTION IMAGER (SMEI)
AND INTERPLANETARY SCINTILLATION (IPS)
3D-RECONSTRUCTIONS OF THE
INNER HELIOSPHERE**

B. V. JACKSON*, P. P. HICK, A. BUFFINGTON,
M. M. BISI[†] and J. M. CLOVER

*Center for Astrophysics and Space Sciences,
University of California, San Diego
9500 Gilman Dr. #0424, La Jolla, CA 92093-0424, U.S.A.*

**bvjackson@ucsd.edu*

http://smei.ucsd.edu/ or http://ips.ucsd.edu/

[†]mmbisi@ucsd.edu

M. TOKUMARU

*Solar-Terrestrial Environment Laboratory, Nagoya University
Furo-cho, Chikusa-ku, Nagoya 464-8601, Japan*

http://stesun5.stelab.nagoya-u.ac.jp/index-e.html

tokumaru@stelab.nagoya-u.ac.jp

The Solar Mass Ejection Imager (SMEI) direct white-light data as well as higher-level data products are available on our UCSD Website at <http://smei.ucsd.edu/> from first light in early February 2003 to nearly the present day. These analyses provide densities in the inner heliosphere, show many familiar CMEs in three dimensions (3D) during this interval, and provide animations and individual images of them. This 3D analysis is enhanced by use of interplanetary scintillation (IPS) velocity observations to help provide the overall form of the structures reconstructed. Our time-dependent 3D reconstruction technique is discussed, and the different ways we test and validate these 3D results. These checks include both internal consistency checks, and comparisons with *in situ* measurements at various near-Earth spacecraft, at Ulysses, at the STEREO spacecraft, and from magnetic field data at Mars.

1. Introduction

The Solar Mass Ejection Imager (SMEI)¹⁻² was launched 6 January 2003 on the Air Force Space Test Program satellite *Coriolis*. The instrument consists of three baffled cameras whose $3^\circ \times 60^\circ$ fields of view are aligned in the long

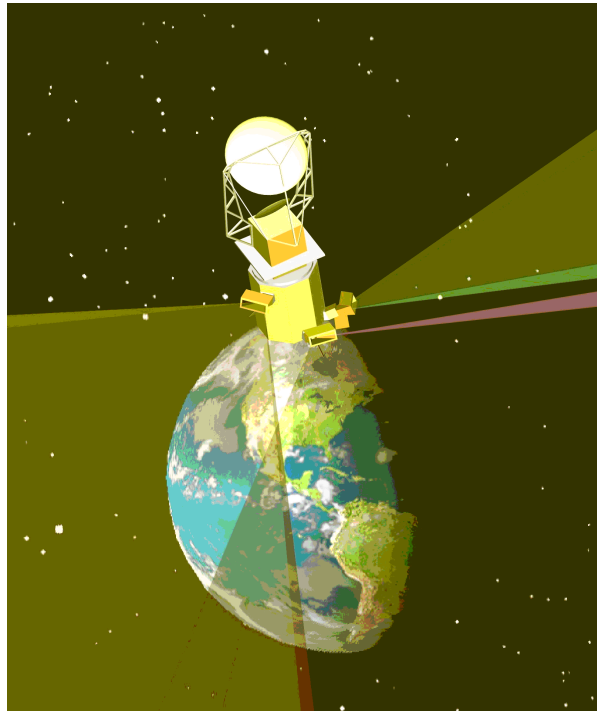


Fig. 1. SMEI is depicted on the Coriolis spacecraft in its terminator polar orbit at 840 km with an orbital inclination of 98° . SMEI looks away from the Earth at 30° above the local horizontal to avoid sunlight reflected from the Earth and from the *Windsat* radiometer antenna situated at the top of the Coriolis spacecraft. The fields of view of the three cameras (each shown as shaded wedges extending from the satellite in this artist's impression) together cover nearly 160° of sky and, as the instrument orbits Earth, sweep out nearly all the sky around it.

dimension to achieve a combined $\sim 160^\circ$ wide field of view that scans most of the sky every 102-minute orbit (Fig. 1). The cameras view the heliosphere in Thomson-scattered light with $\sim 0.5^\circ$ angular resolution. Approximately 4500 four-second exposure CCD-camera data frames per orbit as in Fig. 2a are combined into a map of the sky as shown in Fig. 2b. Calibration of the SMEI data to an absolute level of $\sim 4\%$ using known star brightness has been accomplished.³ Using a combination of three dimensional (3D) reconstruction and image-analysis techniques, SMEI observations quantify the extents of transient structures and their interactions with each other and with slow-moving ambient solar wind. These techniques have mapped the 3D extents of the 28 October 2003 halo coronal mass ejection (CME) and

Solar Mass Ejection Imager (SMEI)

341

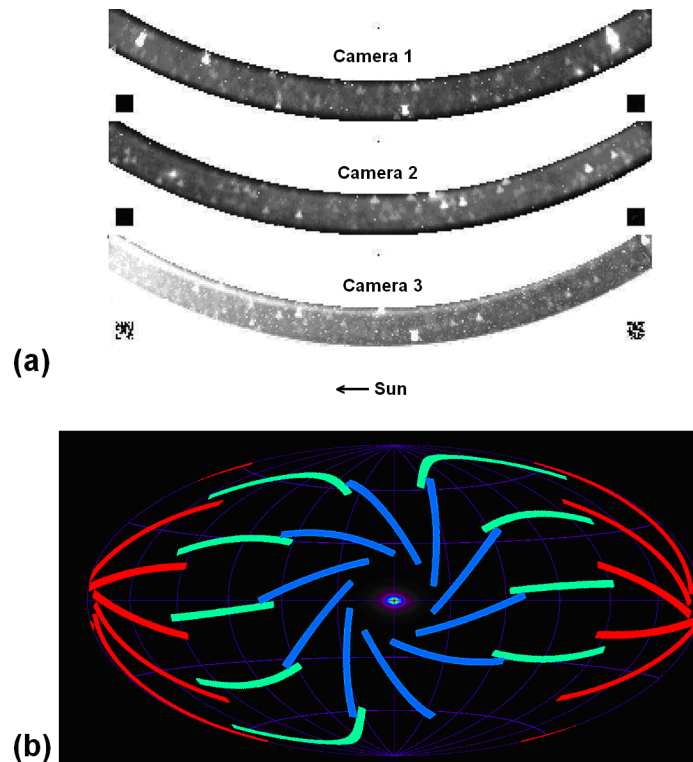


Fig. 2. (a) $3^\circ \times 60^\circ$ image frames from each of the three SMEI cameras. Camera 1 (top) views farthest from the Sun; camera 3 (bottom) closest, with the Sun towards the left in each frame. (b) Full-sky Hammer-Aitoff projection showing the placement of a sample of SMEI camera image frames with the Sun centered in the projection (in October). About 4500 frames per orbit fill in the sky in a clockwise direction every 102 minutes. Camera 1 is shown in red, Camera 2 is in green, and Camera 3 is in blue.

its interplanetary counterpart (ICME) in low resolution and determined its mass.⁴ Other studies that have included interplanetary scintillation (IPS) observations⁵ have mapped the 3D extent of the high velocity structure surrounding the 28 October 2003 ICME and determined the energy present in its outward-flowing material. These same techniques, using a combination of SMEI and IPS data from the Solar-Terrestrial Environment Laboratory (STELab) (Fig. 3) radio antennas,⁶ have also been used to map both the energy and mass of a sequence of halo CMEs that erupted from the Sun on 27–28 May 2003.⁷ IPS analyses alone have been used to determine the structure location, mass, and solar wind speeds from ICMEs^{5,8} and,



Fig. 3. STELab IPS radio array (one of four now operating) near Mt. Fuji. The arrays used singly measure scintillation intensity (or g-value) for about 50 radio sources each day. Scintillation signals cross-correlated between arrays give a robust IPS velocity determination.

by combining both mass and speed, Jackson *et al.*⁹ demonstrated that IPS plasma ram pressure measurements from Mars Global Surveyor (MGS) magnetometer observations compared satisfactorily with these analyses.

The University of California, San Diego (UCSD) time-dependent tomographic analysis that allows solar wind temporal variations to be mapped in 3D is discussed in this article. This current analysis fits data in essentially the same manner for SMEI, IPS, or a combination of these data sets in the 3D-reconstructions. Several of the different tools and error analysis techniques we have developed to certify the 3D reconstruction results are shown. We give examples of these analyses for specific events from both data sets, and using combinations of them. These analyses are also compared with *in-situ* measurements and other remote-sensing observations for specific events. The analysis programs using IPS data from STELab or from SMEI now reside at the Community Coordinated Modeling Center (CCMC) at the Goddard Space Flight Center for use by others, and so this article serves as an explanation for, and the caveats present in using these analysis routines at the CCMC.

This article uses the term ‘CME’ in reference to a sequence of events in the low corona as viewed in the Solar and Heliospheric

Observatory (SOHO) Large-Angle Spectroscopic COronagraph (LASCO)¹⁰ or the twin Solar-TERrestrial RELations Observatory (STEREO)¹¹ near-Sun coronagraph observations, but in keeping with the now common terminology for these, describes these events in the interplanetary medium as ‘ICMEs’; the switch occurring when this material is viewed by SMEI and in IPS observations and measured *in situ* near Earth.

Section 2 describes the time-dependent tomographic analysis routines developed by our group at the University of California, San Diego (UCSD) for fitting SMEI brightness, and STELab IPS velocity and g -level data. Section 3 presents examples of these analyses for the 27–28 May 2003 CME/ICME, and shows some of the measurement techniques we have developed to certify that these analyses are accurate. Section 4 gives examples of these results with *in situ* measurements and remote-sensing observations. We conclude in Section 5.

2. 3D-Reconstruction Analysis

Computational aspects of the UCSD 3D-reconstruction program have been discussed in other articles over the past decade.^{12–15} These analyses and references therein describe early versions of the analysis that use the assumption that the heliosphere corotates. In more recent articles,^{4,5,7,9,16,17} the assumption that heliospheric structure corotates has been relaxed. In this latter modification of the technique, described more fully here, line-of-sight segments and their 3D weights are projected back in space and time to a solar wind inner boundary (a source surface) that is set at a height below the closest approach of all lines of sight to the Sun (usually $15 R_s$). Each line of sight is followed out to typically 2AU from the Earth and projected to the source surface consistent with the velocity and interactions present in the solar wind model.

In current analyses the inversion process updates boundary conditions for the kinematic 3D solar wind model to better fit observations using a least-squares fitting procedure. This procedure minimizes the differences between modeled and observed brightness, or modeled and observed IPS g -value and velocity, or a combination of these. As explained elsewhere,^{7,18} unlike IPS g -level, it is not possible to distinguish the slowly-varying Thomson-scattering signal due to the ambient solar wind from the large and very bright zodiacal light signal. Because of this, the mean value for this ambient is modeled using the average *in-situ* density measured

from the mean solar wind value at 1 AU throughout the period of the observation.

A least-squares fitting program developed specifically for this type of analysis inverts the weighted, projected model values on the two-dimensional (2D) inner boundary source surface at the different time steps to provide solar wind model outflow parameters. The model values are directly inverted on the source surface at the discrete source surface times to give new solar wind parameter values; these are converged for each data set.

In the least-squares fitting process, ratios of modeled-to-observed values and a modeled-to-observed chi-squared are monitored to indicate a rate of convergence for this interval. Velocity and density corrections to the 3D model are made separately. First, the inversion changes are made to previous velocity boundary conditions on the inner boundary surface. Second, the 3D solar wind model is updated and new projected locations of each line-of-sight point on the inner-boundary surface are determined. Third, inversion changes are made to previous density boundary conditions on the inner boundary surface. Finally, the 3D model is again updated with all the newest boundary values.

The Carrington maps of velocity and density at the inner boundary are smoothed each iteration using a 2D Gaussian spatial filter that incorporates equal-solar-surface areas, and a Gaussian temporal filter. Locations where insufficient information is available to change the model values are left blank in the final result. For the analysis presented here, the blank areas include sections of heliospheric volume on the opposite side of the Sun from Earth that cannot be observed or reconstructed by SMEI or IPS at the digital resolutions used.

The reconstruction program generally converges to an unchanging model within a few iterations, but is set to operate for 9 iterations to guarantee convergence.¹² For a typical rotation and the digital resolutions of the current SMEI data sets, a set of density and velocity iterations generally takes about fifteen minutes on a 3.0 GHz Intel® Pentium IV™ computer. Normally those IPS-velocity observations and SMEI-brightness lines of sight throughout the period that do not fit within a three-sigma limit of the mean ratio change ascribed at that location by the model (typically $\sim 1\%$ of the SMEI brightness or IPS velocity lines-of-sight) are removed from the data set. This allows a further safeguard for the removal of lines of sight that are outliers which do not fit the model values. We sometimes find that the overall chi-squared fit, for g -level or brightness or velocity,

is reduced when this criterion is imposed. The program then operates for 9 more iterations (18 in total). The solutions are insensitive to the initial model values, and after a few iterations any residual signature of the initial values has disappeared. Other tests¹² show that the 3D reconstruction of a set of artificial observations using a known 3D input reproduces the input.

In the following subsections we go into more detail about the specific numerical algorithms that are used in the SMEI brightness and IPS time-dependent 3D reconstructions. The data used in the 3D reconstructions are often noisy; this necessitates using different smoothing techniques to mitigate the effects of the noise, and to smooth the intermediate steps in the iterative procedure.

2.1. *IPS and Thomson-scattering remote sensing*

This explanation of the algorithm was given originally in Hick and Jackson,¹⁵ and is adapted for the current analysis in the time-dependent form described here. The derivation presented here closely follows this previous work but is altered after the present Eq. 11 to include time-dependent tomography. The present formulae retain IPS g^2 , but now also include the Thomson-scattering measured brightness B .

The observational data used in the IPS tomographic reconstruction are the IPS g -level (or ‘disturbance factor’) and IPS velocity V_{IPS} observations. Each observation represents a line-of-sight integration through the solar wind in the inner heliosphere. To date we have used g -level data from the IPS arrays in Cambridge (UK), Ooty (India), and Nagoya (Japan); V_{IPS} data have been available from Nagoya and Ooty. The purpose of the reconstruction is to create a model 3D heliosphere (i.e. a density and velocity distribution) that reproduces these observations as well as possible. The reconstruction uses an iterative scheme to minimize the differences between actually observed and calculated model values. Since the reconstruction only involves the solar wind density n and the (radial) solar wind outflow velocity V , the observed quantities g and V_{IPS} need to be related to these two solar wind parameters. The g -level is related to the scintillation index m :

$$g = m/\langle m \rangle, \quad (1)$$

where m is the instantaneous observed scintillation index for an IPS source; $\langle m \rangle$ is the expected “quiet” scintillation index, based on an average of

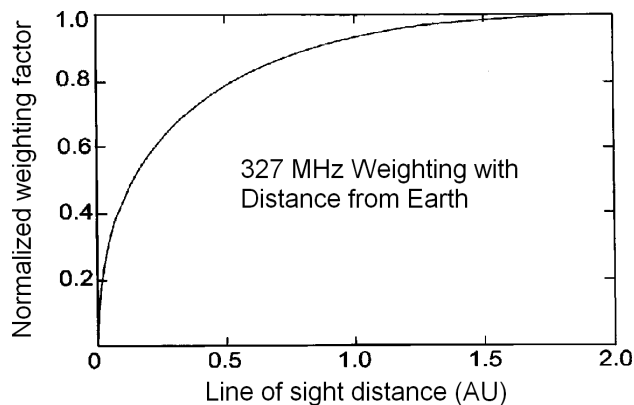


Fig. 4. IPS 327 MHz line of sight weighting with distance from Earth as described in Jackson *et al.*¹²

past source observations as a function of solar elongation, and g depends only weakly on elongation (or heliocentric distance). The scintillation index m is related to the small-scale density variations along the line of sight s by:

$$m^2 = \int_0^\infty ds W\rho(s)\delta n(s)^2. \quad (2)$$

The “weight” function $W\rho(s)$

$$W\rho(s) = 2\pi \int_0^\infty q dq \sin^2(q^2 \lambda_O s / (4\pi)) \exp(-\Theta_O^2 q^2 s^2 / 2) q^{-3} \quad (3)$$

as formulated by Young¹⁹ and refined by Kojima *et al.*,¹² depends on observing wavelength λ_O , the angular size of the radio source Θ_O , and the turbulence power spectrum with wave vector q . The same Eq. 3 weak-scattering weighting factor along the line of sight is assumed for fast and slow solar wind, and different solar wind structure. This weighting is given for STELab data assuming a nominal angular source size of 0.1 arc sec (Fig. 4). The small-scale density fluctuations $\delta n(s)$ along the line of sight cause the scintillation. $\delta n(s)$ depends not only on macroscopic properties (solar wind speed, density, magnetic field), but also on microscopic properties associated with turbulence in the solar wind. However, empirical evidence²⁰ suggests that changes in $\delta n(s)$ scale with changes in values of the bulk electron density. Quantitatively we model this behavior by expressing $\delta n(s)$ in terms of the heliocentric distance r and the solar wind

electron density n , or equivalently, the normalized density \hat{n} defined as $\hat{n} = (r/r_0)^2 n$:

$$\delta n(r, \hat{n}) = \delta n_0 (r_0/r)^{2-\beta r} (\hat{n}/n_0)^{\beta n}. \quad (4)$$

A value for r_0 of 1 AU normalizes results to observations at this distance from the Sun.¹⁴ The tomography is calculated using values for the powers $\beta n \approx 0.5^{2.3}$ and $\beta r \approx 0$ that are derived by iteratively fitting remote-sensing results to *in-situ* solar wind velocity and density measurements.^{12,20} The mean scintillation index $\langle m \rangle$ (and hence the g -level) depends on parameters \hat{n}^{mean} and δn_0^{mean} describing the density and density fluctuation in the “average” background solar wind.

The IPS velocity is defined in terms of the same weight function and small-scale density fluctuations,

$$V_{\text{IPS}} = \int_0^\infty ds W \rho(s) \delta n(s)^2 V_\perp(s) / \int_0^\infty ds W \rho(s) \delta n(s)^2. \quad (5)$$

Here, V_\perp is the component of the solar wind velocity perpendicular to the line of sight at a distance s from the observer. The most accurate calculation of V_{IPS} uses the cross correlation of the IPS signals at different IPS stations.^{6,14} The above expression is consistent with this more accurate calculation to within $\sim 10 \text{ km s}^{-1}$ while significantly reducing the required computational resources.¹⁴

We introduce a few simplifying definitions to generate the equations for g and V_{IPS} that are implemented in our numerical algorithm. First, write the background solar wind density \hat{n}^{mean} (needed to calculate $\langle m \rangle$) as:

$$\hat{n}^{\text{mean}}(s) = n_{\text{mean}} \bar{n}_{\text{mean}}(s). \quad (6)$$

The constant n_{mean} sets the absolute density scale. \bar{n}_{mean} is a dimensionless function defining the shape of the mean background solar wind density distribution. Also define η as the normalized density \hat{n} to absorb the constants δn_0 , δn_0^{mean} , and n_{mean} :

$$\eta = (\delta n_0 / \delta n_0^{\text{mean}})^{1/\beta n} \hat{n} / n_{\text{mean}}. \quad (7)$$

This “modified normalized density” will be useful later in the discussion of the kinematic solar wind model (Section 2.3.1). Define the “ γ function”:

$$\gamma = \eta^{2\beta n}. \quad (8)$$

Finally, define a new weight function $W\sigma$ that absorbs the dependence on heliocentric distance:

$$W\sigma(s, \beta r) = W\rho(s)r(s)^{-2(2-\beta r)}. \quad (9)$$

With these definitions g -level and IPS speed V_{IPS} become:

$$g^2 = \int_0^\infty ds W\sigma(s, \beta r)\gamma(s) / \int_0^\infty ds W\sigma(s, \beta r)(\bar{n}_{\text{mean}}(s))^{2\beta n}, \quad \text{and} \quad (10)$$

$$V_{\text{IPS}} = \int_0^\infty ds W\sigma(s, \beta r)\gamma(s)V(s) \sin \chi(s) / \int_0^\infty ds W\sigma(s, \beta r)\gamma(s) \quad (11)$$

where we put $V_\perp(s) = V(s) \sin \chi(s)$, and assume $V(s)$ is radial. $\chi(s)$ is the angle between the direction to the Sun and to the Earth from the position at distance s along the line of sight. In Eq. (10) we usually set $n_{\text{mean}} = 1$; i.e. we assume a background solar wind density with a $1/r^2$ drop-off.

In the analysis of brightness from Thomson scattering as given in Jackson and Hick,¹⁸ and adapted for this description:

$$B = \int_0^\infty ds n(s)Wt(s), \quad (12)$$

where $n(s)$ is the bulk electron density per cubic centimeter, at distance s in cm, along the line of sight; $Wt(s)$, the scattered intensity per electron, serves as a brightness ‘weight factor’ for the density. For the large distances from the Sun viewed by SMEI:

$$Wt(s) = 1/2 \sigma_T F_S(s) (r_0/r(s))^2 (2 - \sin^2 \chi(s)), \quad (13)$$

where σ_T is the Thomson-scattering cross section, $F_S(s)$ is the flux received from the solar disk at a distance r_0 , $r(s)$ is the distance of the electron from the Sun, and $\chi(s)$ is the angle between the incident solar radiation from the Sun and the direction of scattering towards the spacecraft instrument viewing the sky.²¹ To evaluate Eq. (13) both $r(s)$ and $\chi(s)$ are evaluated as functions of the distance R of the observer from the Sun, elongation ε of the line of sight, and distance s along the line of sight. Using R , ε , and s as independent variables $Wt(s)$ scales as R^{-2} . For a fixed R and ε , the function $Wt(s)$ has a maximum at $s = R \cos \varepsilon$, and is symmetric around this point. For $\varepsilon < 90^\circ$ the maximum is at the point of closest approach of the line of sight to the Sun. Figure 5 shows the weight function at $\varepsilon = 16^\circ$, 31° , and 90° for $R = 1$ AU.

For tomography based on Thomson scattering brightness rather than g -level, Eq. (12) replaces Eq. (10). Note the structural similarity between

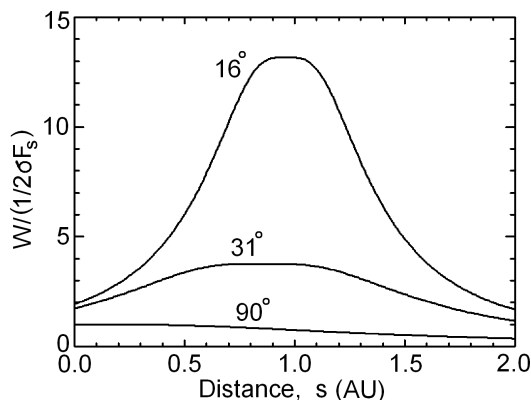


Fig. 5. Thomson-scattering line of sight weighting at three different elongations with distance from the Earth as described in the text (from Jackson and Hick¹⁸).

these equations. The weight ($W\sigma$ and Wt) captures the line-of-sight geometry and the microscopic scattering physics and γ (implicitly, Eq. 10), and n (explicitly, Eq. 12) describes the dependency on bulk solar wind density. This similarity allows us to apply the same algorithm to both IPS and Thomson scattering tomography.

There are three undetermined functions in these equations: γ (or equivalently in the case of IPS, the normalized density \hat{n}), the radial solar wind outflow speed V , and \bar{n}_{mean} , the shape of the background normalized solar wind density. In the case where both Thomson-scattering and IPS is used in the same tomographic routine, γ is assumed directly related to n by use of Eqs. (7) and (8), and the equivalence of γ to \hat{n} . The first two of the unknown functions, γ (or n) and V , are our primary interest in the time-dependent 3D reconstructions described in the following sections. The reconstruction problem can be formulated as follows: for a given shape \bar{n}_{mean} (specified over the heliospheric volume of interest), and for a given set of g -level and V_{IPS} observations, find the functions γ (or equivalently n) and V that best fit these observations.

Several points can be made about Eq. (10) and Eq. (11):

1. g^2 is a more ‘natural’ observational quantity than g itself. Both g^2 and V_{IPS} are described in terms of very similar integrals, with $\gamma(s)$ and $V(s)\sin\chi(s)$ specifying the contribution of a line-of-sight segment at distance s from the observer to the observed g -level and IPS speed, respectively.

2. The numerator and denominator for g and V_{IPS} have the same dependence on heliocentric distance; thus V_{IPS} and also g (except with unusual radially structured solar wind) will be nearly independent of solar elongation.
3. The influence of both n_{mean} and βn has been reduced to determining the density scale (Eq. 7) together with the unknown constants δn_0 and δn_0^{mean} . The solution for γ and V depends explicitly on βr , which controls the weighting for the line-of-sight contribution $\gamma(s)$ and $V(s) \sin \chi(s)$.
4. For a given shape \bar{n}_{mean} , if the pair of functions \hat{n}, V is the solution for a specific n_{mean} , then the pair $\alpha \hat{n}, V$ is the solution for αn_{mean} for any constant α .

The last point implies that for a given set of g -level and V_{IPS} observations, the solution for the normalized density \hat{n} is determined only up to a constant, i.e. the absolute density scale of the solution cannot be determined from the tomographic reconstruction itself. This is not surprising: the g -level, our proxy for the solar wind density, is only a relative statement about the state of the solar wind along the line of sight to the IPS source as compared with ‘average’ conditions (Eq. 1). What these ‘average’ conditions are must be established using external information. For instance, the density scale can be calibrated against solar wind densities observed *in situ* at 1 AU near Earth. This external calibration defines the relationship between γ and n in Eqs. (7) and (8), and hence also implicitly defines the constants δn_0 and δn_0^{mean} .

Unlike the g -level, Thomson-scattering (Eq. 12) changes in brightness determine the absolute scale of electron density variations $\Delta n(s)$. However, in our tomographic algorithm, the total density is needed in the solar wind model. There is a difficulty with Thomson-scattering brightness in determining the ambient density because only a tiny percentage ($\leq 1\%$) of the total brightness of the heliosphere arises from sunlight scattering off ambient solar wind. The far larger fraction is due to the zodiacal light, scattering from interplanetary dust. If we divide the solar wind density into two components:

$$n(s) = n_{\text{quiet}}(s) + \Delta n(s) \quad (14)$$

then the differential Thomson scattering measurements provide information about the variable part $\Delta n(s)$. Because of this, the mean value for the ambient $n_{\text{quiet}}(s)$ needs to be established externally and determined over s , the distance from the observer. This is usually accomplished using

in situ density measured from the mean solar wind value at 1 AU throughout the Carrington rotation (CR) period of the observation, and mapped everywhere in the heliosphere assuming a radial density fall-off. Finally it is assumed that, at the distance of 1 AU, solar wind speeds provide a constant mass flux throughout a CR regardless of heliographic latitude or longitude. With this modification to the analysis, Thomson scattering intensity can replace g -levels in the tomographic reconstruction. With this caveat, the Thomson-scattering equations and the SMEI results derived from them are determined in a far more straightforward manner and with far fewer assumptions than in the case of the IPS analysis.

2.2. The numerical algorithm

The reconstruction task has been reduced to finding the functions γ (or n) and V for a given set of g -level, V_{IPS} , or B observations satisfying Eqs. (10), (11), or (12). The IPS normalized density \hat{n} follows from γ using Eqs. (7) and (8), or in the case where Thomson scattering brightness is measured, Eq. (14) and a radial fall-off of density currently provides \hat{n} for the determination of V_{IPS} .

2.2.1. Notation: use of subscripts

In the following, subscripts i, j, k , and l are used when a quantity refers to the 3D heliospheric grid (next subsection) in computing the heliospheric γ -function and velocity, and quantities at the source surface (when only i, j , and l appear). The subscript μ is used to identify a line of sight while ν refers to a segment at a certain distance from the observer along the line of sight.

2.2.2. Remote-sensing observations

The reconstruction is based on a set of N_{obs} line-of-sight observations for g -level, IPS velocity V_{IPS} , and Thomson-scattering brightness B . Because there are far more lines of sight from SMEI observations than from the IPS, the heliospheric resolutions obtained from the analyses with the greatest numbers of lines of sight are presumed to dominate, and for this reason there are two different programs used in the reconstructions; one with spatial and temporal resolutions specific for the highest numbers of SMEI lines of sight, and another program that operates at the resolutions of the IPS

data set:

$$(g^2)_\mu^{\text{obs}}, V_{\text{IPS},\mu}^{\text{obs}}, B_\mu^{\text{obs}} \quad (\mu = 1, N_{\text{obs}}) \quad (15)$$

“Model values” are calculated from the latest iterative 3D model of heliospheric γ -function and velocity V , and are compared with the actual observations. The purpose of the reconstruction is to create a model 3D heliosphere that matches these observations as closely as possible. The model values are given by

$$(g^2)_\mu^{\text{mdl}}, V_{\text{IPS},\mu}^{\text{mdl}}, B_\mu^{\text{mdl}} \quad (\mu = 1, N_{\text{obs}}) \quad (16)$$

Each line of sight is subdivided into N_{los} segments of length ds_μ . The segment length is expressed as a constant in units of the Sun-Earth distance. Since for Earth-based observations this distance varies with time, this means that the segment length is slightly different for each line of sight. The distance from observer to the center of each line segment is given by:

$$s_{\nu,\mu} = (\nu - 0.5)ds_\mu \quad (\nu = 1, N_{\text{los}}; \mu = 1, N_{\text{obs}}) \quad (17)$$

Values of line-of-sight segments are normalized to the spatial longitudinal resolution (λ_R) of the reconstructions in degrees such that $ds_\mu = \lambda_R \times r / 200$ for $\lambda_R \leq 10^\circ$ and $N_{\text{los}} = 2r / ds_\mu$, so that for an observer at Earth ($r = 1$ AU) each line of sight extends out about 2 AU.

2.2.3. The solar wind plasma

The grid used in the reconstruction is regular in heliographic longitude, heliographic latitude, heliocentric distance, and time, and is fixed relative to the Sun (i.e. rotates with the sidereal solar rotation rate, P_{sid}). The range of longitudes covered by the grid (360° , i.e. a whole solar rotation), is expressed in terms of the ‘Carrington variable’, c . One unit in a Carrington variable covers 360° in heliographic longitude. The integer part, $\text{int}(c)$, is a conventional CR number, and effectively sets the time period of interest. The fraction is related to the heliographic longitude, $\lambda = 360^\circ \times \{1 - (c - \text{int}(c))\}$.

The range of heliographic longitudes for the grid is set by a start and end “Carrington variable”: c_{beg} and c_{end} . Note that the grid does not need to start at 0° , i.e. at the exact start of a new CR. Associated with the variables c_{beg} and c_{end} are the times, t_{beg} and t_{end} at which the corresponding heliographic longitude crossed the center of the solar disk as

seen from Earth (or, more general, “the observer”). These times determine which observations are used for the reconstruction. E.g. all g -level, V_{IPS} , and brightness observations inside the time interval $[t_{\text{beg}} - t_{\text{marg}}, t_{\text{end}} + t_{\text{marg}}]$ are used. The “safety margin” on each end of the time interval is used to include all observations that can impact the time period of interest.

The latitude grid covers the full range -90° to $+90^\circ$. The radial grid covers the range from the “source surface” at R_s to some outer boundary at R_{max} .

$$\begin{aligned}
 c_i &= c_{\text{beg}} + (i - 1) \times dC & dC &= (c_{\text{end}} - c_{\text{beg}})/(N_c - 1) \quad (i = 1, N_c) \\
 l_j &= -\pi/2 + (j - 1) \times dL & dL &= \pi/(N_l - 1) \quad (j = 1, N_l) \\
 r_k &= R_s + (k - 1) \times dR & dR &= (R_{\text{max}} - R_s)/(N_r - 1) \quad (k = 1, N_r) \\
 t_l &= (t_{\text{beg}} - t_{\text{marg}}) + (l - 1) \times dT & dT &= (t_{\text{end}} - t_{\text{beg}} + 2t_{\text{marg}})/ \\
 & & & (N_t - 1) \quad (l = 1, N_t)
 \end{aligned} \tag{18}$$

Typical values for the SMEI grid parameters are $R_s = 15$ solar radii, $R_{\text{max}} = 3 \text{ AU}$, $dR = 0.1 \text{ AU}$, $dC = 1/54$ (i.e. 6.67° in heliographic longitude), $dL = 6.67^\circ$, and $dT = 0.5$.

The tomography reconstructs the 3D heliospheric γ -function (and its associated normalized density \hat{n} , or n) and velocity V in grid points of Eq. (18):

$$\gamma_{i,j,k,l} \text{ or } n_{i,j,k,l}, V_{i,j,k,l} (i = 1, N_c; j = 1, N_l; k = 1, N_r; l = 1, N_t) \tag{19}$$

The lower boundary of the heliospheric grid ($k = 1$), the “source surface”, plays a crucial role in the tomographic reconstruction. The γ -function or n and velocity at the source surface are simply the above equation evaluated only for $k = 1$, but with the other indices evaluated over the full range of values. Specifying the content of these two maps at every time t_l initializes the reconstruction; each iteration is completed by updating them.

2.2.4. Discretization of the line-of-sight integrals

The calculation of model g -level and IPS velocity V_{IPS} , observations requires an integration through the model heliosphere along the same directions (lines of sight) as the actual observations (Eqs. 10, 11, and 12). In discrete

form this becomes:

$$(g^2)_\mu^{\text{mdl}} = \sum_{\nu=1}^{N_{\text{Ios}}} H_{\nu,\mu} \gamma_{\nu,\mu} \quad \text{or} \quad (n)_\mu^{\text{mdl}} = \sum_{\nu=1}^{N_{\text{Ios}}} H_{\nu,\mu} \gamma_{\nu,\mu} \quad (20)$$

with weight factors

$$H_{\nu,\mu} = \sigma_{\nu,\mu} / \sum_{\nu=1}^{N_{\text{Ios}}} \sigma_{\nu,\mu}, \quad (21)$$

and

$$V_{\text{IPS},\mu}^{\text{mdl}} = \sum_{\nu=1}^{N_{\text{Ios}}} K_{\nu,\mu} V_{\nu,\mu} \sin \chi_{\nu,\mu} \quad (22)$$

with weight factors

$$K_{\nu,\mu} = \sigma_{\nu,\mu} \gamma_{\nu,\mu} / \sum_{\nu=1}^{N_{\text{Ios}}} \sigma_{\nu,\mu} \gamma_{\nu,\mu}, \quad (23)$$

and where

$$\sigma_{\nu,\mu} = \sigma(s_{\nu,\mu}) = \rho(s_{\nu,\mu}) r_{\nu,\mu}^{-2(2-\beta r)}. \quad (24)$$

The μ -dependence of $s_{\nu,\mu}$ enters through the μ -dependence of ds_μ (Eq. 17). The function $\rho(s)$ does not depend on the line-of-sight orientation (i.e. the elongation), but does depend on the distance along the line of sight.

The heliospheric γ or n function and velocity in all line-of-sight segments

$$\gamma_{\nu,\mu}, \text{ or } n_{\nu,\mu}, V_{\nu,\mu} \quad (\nu = 1, N_{\text{Ios}}; \mu = 1, N_{\text{obs}}) \quad (25)$$

are obtained by linear interpolation on the 4D γ or n function and velocity (Eq. 19) at the center positions (Eq. 17) of all line-of-sight segments.

2.3. The iterative process

The iterative process is started by specifying γ or n function values and velocity V at the 3D (spatial, time) source surface. Using these source surface values the 4D γ function values and velocities (Eq. 19) in the heliospheric grid (Eq. 18) are obtained by applying a solar wind model for the propagation of mass from the source surface out into the heliosphere.

We assume radial outflow and apply simple kinematic arguments to conserve mass and mass flux (Section 2.3.1). At this stage also “traceback” information is accumulated which connects each heliospheric grid point to its “source location” at the source surface.

Model line-of-sight observations (Eq. 16) are calculated by integrating along the appropriate directions through the 4D heliosphere, and include taking into account the light travel time of photons originating at different distances from the observer. These model values are compared with the actual observations (Eq. 15). This comparison provides the main convergence criterion for the iterative process. The observed-to-modeled ratios for all lines of sight will be used to determine the source surface update, completing the iteration.

All line-of-sight segments are projected back to the source surface using the “traceback” information, carrying along the observed-to-modeled ratio of the line of sight they belong to. At the source surface all the segments of all lines of sight are assigned to the nearest grid point. The γ -function or n and velocity in the grid point are then updated by combining observed-to-modeled ratios of all line of segments assigned to the grid point.

We now follow the main steps in this process in detail.

2.3.1. *The kinematic solar wind model*

Given are the γ function values and velocities on the source surface at heliocentric distance $r_0 = R_s$. From these we need to reconstruct the γ function values and velocities at “higher levels”, i.e. heliocentric distances r_k ($k = 2, N_l$). The problem is solved by induction.

Given the γ values and velocities at level k are available, the γ values and velocity at level $k + 1$ need to be determined. The connection between the levels is established using simple kinematic arguments based on conservation laws. Currently we use conservation of mass and mass flux (though other choices, such as conservation of momentum, are easily implemented). Each grid point i, j, l on level k (Eq. 19) represents a parcel of mass with a normalized density $\tilde{n}_{i,j,k,l}$ (related to $\gamma_{i,j,k,l}$ through Eqs. 7 and 8) and velocity $V_{i,j,k,l}$. The parcel of mass is assumed to travel radially outward at the local speed. When it arrives at level $k + 1$ at a later time it has a normalized density $\hat{n}_{i,j,k,l}$ and velocity $\hat{V}_{i,j,k,l}$. The conservation laws for the parcels of material (mass and mass flux, respectively) are:

$$\tilde{n}_{i,j,k,l} = \hat{n}_{i,j,k,l}; \quad \tilde{n}_{i,j,k,l} V_{i,j,k,l} = \hat{n}_{i,j,k,l} \hat{V}_{i,j,k,l} \quad (26)$$

In the corotating heliographic coordinate system the parcel will have moved to a larger Carrington variable (smaller heliographic longitude). The parcel will arrive at level $k + 1$ at Carrington variable:

$$\hat{c}_{i,j,k,l} = c_{i,j,k,l} + dR/V_{i,j,k,l}P_{\text{sid}} \quad (27)$$

at time

$$\hat{t}_{i,j,k,l} = t_{i,j,k,l} + dR/V_{i,j,k,l} \quad (28)$$

where P_{sid} is the sidereal rotation period of the Sun where $dR = r_{k+1} - r_k$. Note that the parcel only shifts in longitude and time, not in heliographic latitude using the current conservation laws. The position $\hat{c}_{i,j,k,l}$ and time $\hat{t}_{i,j,k,l}$ place the parcel somewhere in between grid points (in space and time) at level $k + 1$. Here we will only discuss longitude (and its increment i), but in fact a similar interpolation is also made in time. Let the new grid points be (i_{near}, j) and (i_{far}, j) , where $|i_{\text{near}} - i_{\text{far}}| = 1$. Let grid point (i_{near}, j) be closest to $\hat{c}_{i,j,k,l}$, and define the difference in Carrington variable $\delta\hat{c}_{i,j,k,l} = |\hat{c}_{i,j,k,l} - \hat{c}_{i_{\text{near}},j,k,l}|$. At level $k+1$ each parcel of mass is split up in two fractions, which are assigned to the neighboring grid points (i_{near}, j) and (i_{far}, j) . A fraction $f_{\text{near}} = 1 - \delta\hat{c}_{i,j,k,l}$ is assigned to (i_{near}, j) , and the remaining fraction $f_{\text{far}} = \delta\hat{c}_{i,j,k,l}$ is assigned to (i_{far}, j) . The normalized density and velocity at each grid point (i, j, l) , at level $k + 1$ are obtained by averaging all nearest parcel fraction values weighted according to the fraction, in space and time, assigned to a given grid point.

The displacements $\hat{c}_{i,j,k,l} - c_{i,j,k,l}$ and $\hat{t}_{i,j,k,l} - t_{i,j,k,l}$ from Eq. (27) and Eq. (28) respectively are used to construct a ‘‘traceback matrix’’ S^c and S^t that connects each heliospheric grid point in space and time to its origin at the source surface (i.e. the point on the source surface which lies on the same stream line as the grid point), and for the Carrington variable this is:

$$c_{i,j,k,l}^{\text{source}} = c_{i,j,k,l} + S_{i,j,k,l}^c \quad (29)$$

For radial outward flow (currently assumed), the value of $S_{i,j,k,l}^t$ is simply the time difference between the Carrington variable at the upper grid point and the Carrington variable at the source surface. This ‘traceback matrix’ is needed in the final phase of the iteration to project the line-of-sight observations back to the source surface (Section 2.3.3).

2.3.2. Convergence criterion and rejection of outliers

Improving the model from one iteration to the next is based on a comparison of model observations (Eq. 16) and actual observations (Eq. 15). Error estimates for g -levels, IPS velocities V_{IPS} , and brightness B are defined as:

$$\sigma_g^2 = N_{\text{obs}}^{-1} \sum_{\mu=1}^{N_{\text{obs}}} (\tau_{\mu}^g - 1)^2 \quad (30)$$

$$\sigma_{V_{\text{IPS}}}^2 = N_{\text{obs}}^{-1} \sum_{\mu=1}^{N_{\text{obs}}} (\tau_{\mu}^{V_{\text{IPS}}} - 1)^2 \quad (31)$$

$$\sigma_B^2 = N_{\text{obs}}^{-1} \sum_{\mu=1}^{N_{\text{obs}}} (\tau_{\mu}^B - 1)^2 \quad (32)$$

and where we define the ratios of observed and model values:

$$\tau_{\mu}^g = (g^2)_{\mu}^{\text{obs}} / (g^2)_{\mu}^{\text{mdl}} \quad (33)$$

$$\tau_{\mu}^{V_{\text{IPS}}} = V_{\text{IPS},\mu}^{\text{obs}} / V_{\text{IPS},\mu}^{\text{mdl}} \quad (34)$$

$$\tau_{\mu}^B = B_{\mu}^{\text{obs}} / B_{\mu}^{\text{mdl}} \quad (35)$$

These quantities (Eqs. 30–32) give estimates of the relative deviation of model values and actual observations, and are the best convergence criteria available. These should move closer to zero from iteration to iteration.

The relative differences of model and actual observations for individual lines of sight (normalized to the “average deviation” for all sources; Eqs. 30–32)

$$\delta g_{\mu} = (\tau_{\mu}^g - 1) / \sigma_g \quad (36)$$

$$\delta V_{\text{IPS},\mu} = (\tau_{\mu}^{V_{\text{IPS}}} - 1) / \sigma_{V_{\text{IPS}}} \quad (37)$$

$$\delta B_{\mu} = (\tau_{\mu}^B - 1) / \sigma_B \quad (38)$$

are used as a criterion to flag individual observations as bad. If after a specified number of iterations the relative difference for an observation is above a certain threshold (typically set to 3 for g -level, V_{IPS} , and B observations) this is used to justify throwing out the data point. The iterative process is then restarted with these “outlier” data points removed.

2.3.3. *Projection to the source surface*

To finish the iteration, the results from Section 2.3.2. need to be translated to the source surface. Let the heliographic coordinates of the line-of-sight segments (Carrington variable, heliographic latitude, heliocentric distance, and time respectively) be:

$$c_{\nu,\mu}, l_{\nu,\mu}, r_{\nu,\mu}, t_{\nu,\mu}. \tag{39}$$

This location is ‘traced back’ to the source surface using the “traceback matrix” S (from Eqs. 28 and 29). The traceback value at the line-of-sight segment $S_{\nu,\mu}$ is calculated from a linear interpolation on neighboring heliospheric grid points. The source location is then defined by:

$$c_{\nu,\mu}^{\text{source}} = c_{\nu,\mu} + S_{\nu,\mu}^c; \quad l_{\nu,\mu}^{\text{source}} = l_{\nu,\mu}; \quad r_{\nu,\mu}^{\text{source}} = R_s; \quad t_{\nu,\mu}^{\text{source}} = t_{\nu,\mu} + S_{\nu,\mu}^t. \tag{40}$$

2.3.4. *Source surface updates*

The projected locations (Eq. 40) of all line-of-sight segments will be scattered across the source surface. Figure 6 shows samples of these

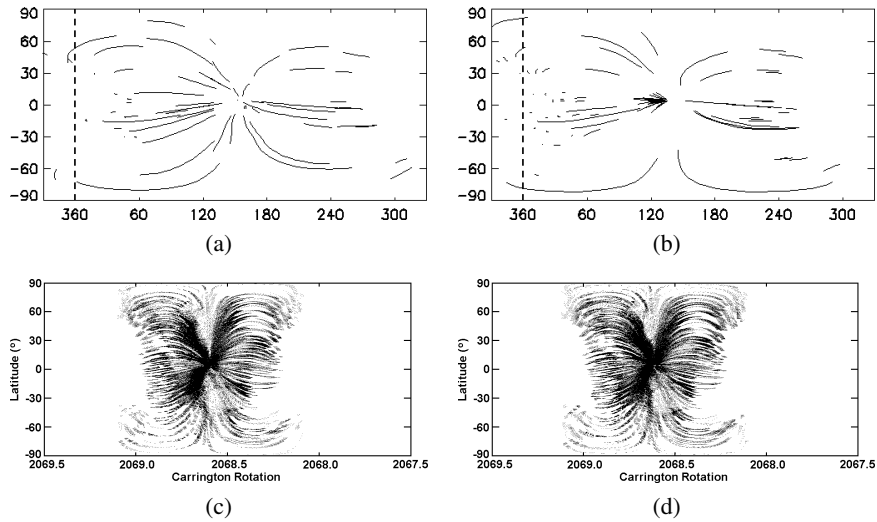


Fig. 6. Samples from the time-dependent analysis of line-of-sight segments projected onto a Carrington map. Lines of sight begun in one map often complete in another (a) and (b) STELab velocity line-of-sight projections on 14 and 15 July 2000 shown for one 360° Carrington rotation. (c) and (d) SMEI line-of-sight projections for two half-day intervals in the beginning of April, 2008.

projected line-of-sight segments. We show adjacent periods of the IPS 3D reconstructions in Fig. 6a and 6b, and two adjacent periods from the SMEI 3D reconstructions in Fig. 6c and 6d. For each grid element (i, j, l) at the source surface, all segments located within one half grid spacing and time of the grid element are collected:

$$\begin{aligned} c_{i,j,l} - dC/2 \leq c_{\nu,\mu}^{\text{source}} \leq c_{i,j,l} + dC/2; \quad l_{i,j,l} - dL/2 \leq l_{\nu,\mu}^{\text{source}} \\ \leq l_{i,j,l} + dL/2; \quad \text{and} \quad t_{i,j,l} - dT/2 \leq t_{\nu,\mu}^{\text{source}} \leq t_{i,j,l} + dT/2. \end{aligned} \quad (41)$$

The ratios in Eqs. 33–35 for these line-of-sight segments are then used to update the source surface γ function or n and velocity. The group of segments near bin (i, j, l) is defined by a group of pairs:

$$(\nu_a, \mu_a), \quad a = 1, N_{i,j,l}^{\text{segments}} \quad (42)$$

The ratios for this group of segments are combined in a weighted mean to obtain a correction factor to the source surface values:

$$\begin{aligned} \gamma_{i,j,l}^{\text{new}} / \gamma_{i,j,l}^{\text{old}} &= \frac{\sum_{a=1}^{N_{i,j,l}^{\text{segments}}} H_{\nu_a, \mu_a} \tau_{\mu_a}^g}{\sum_{a=1}^{N_{i,j,l}^{\text{segments}}} H_{\nu_a, \mu_a}} \\ n_{i,j,l}^{\text{new}} / n_{i,j,l}^{\text{old}} &= \frac{\sum_{a=1}^{N_{i,j,l}^{\text{segments}}} H_{\nu_a, \mu_a} \tau_{\mu_a}^n}{\sum_{a=1}^{N_{i,j,l}^{\text{segments}}} H_{\nu_a, \mu_a}} \\ V_{i,j,l}^{\text{new}} / V_{i,j,l}^{\text{old}} &= \frac{\sum_{a=1}^{N_{i,j,l}^{\text{segments}}} K_{\nu_a, \mu_a} \tau_{\mu_a}^V}{\sum_{a=1}^{N_{i,j,l}^{\text{segments}}} K_{\nu_a, \mu_a}} \end{aligned} \quad (43)$$

Thus, for each segment included in the sum the correction factor τ is weighted proportional to the weight it had in the calculation of the model observation.

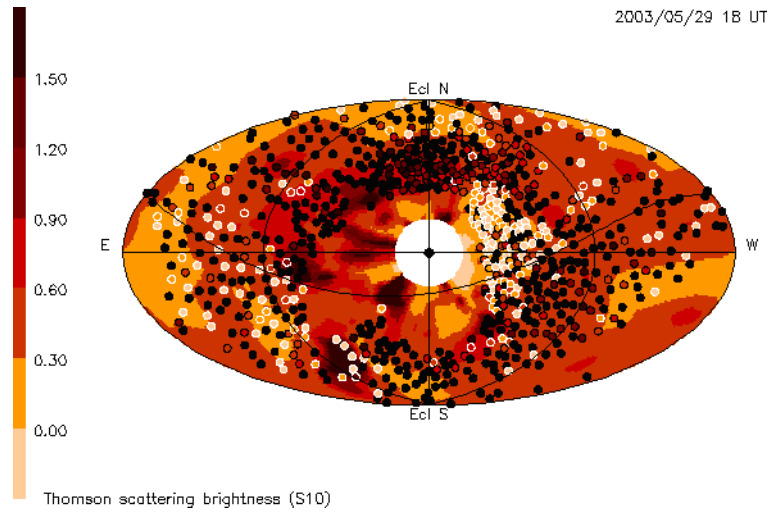
Before continuing with the next iteration the new source-surface values are smoothed by applying a circular spatial (relative to a grid point on the source surface), and a temporal Gaussian filter as mentioned earlier across the entire source surface^{4,5,7}. The purpose of this is mainly to ‘dampen’ the solution, and thereby improve the stability of the iteration process.

3. Analysis Examples

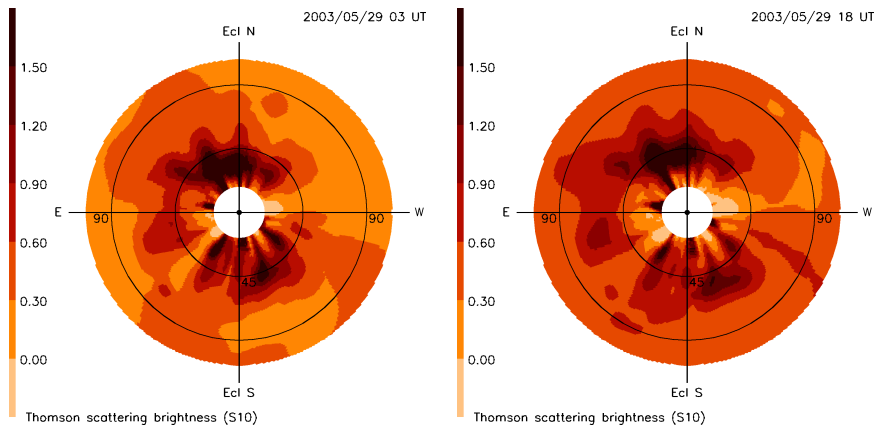
SOHO/LASCO C3 coronagraph images of 27 and 28 May 2003 show several halo CMEs with considerable structure and mass combined with

background coronal features. The first of these events moves out slowly such that the latter, having started about 18 hours later but having over twice the outward expansion rate, has caught up with the first on their way to Earth.

The 27–28 May 2003 CME sequence was one of the first recognized in direct SMEI images as a halo event observed in the interplanetary medium.^{2,22} The SMEI direct images contain numerous artifacts; to remove these effectively for observing ICMEs takes considerable effort (see, e.g. Jackson *et al.*^{2,7}) for a more detailed explanation of how the removal of many of the artifacts present in the SMEI data is accomplished in order to prepare them for the 3D reconstruction analysis). Figure 7 shows a sky map presentation from the 27–28 May 2003 CME sequence. Figure 7a shows where the lines of sight within ± 1.5 hours of the time period of the Hammer-Aitoff (full sky) map presentation are placed to produce the reconstruction coverage. 7b and 7c present a sequence of 3D-reconstructed fisheye sky maps as in Jackson *et al.*⁷ and show the progression of the 27–28 May 2003 ICMEs outward in 2D sky maps. The sky maps are derived from the 3D reconstructed density volumes that have been fit to the observed SMEI data as described in Section 2. The times given in Fig. 7 are instantaneous times interpolated to the appropriate value from the (a) reconstruction analyses. The brightness includes the r^{-2} heliospheric density fall-off, and thus provides brightness as observed in direct images. The sky maps from the tomographic modeling have a $3.3 \text{ e}^{-} \text{ cm}^{-3}$ base at 1 AU removed from them that is also modeled with an r^{-2} heliospheric density fall-off (see text Section 2.1.), and show excursions from a mean of zero, in order to match direct images from SMEI, where all but the changing brightness has been removed. Since the fit to a heliospheric solar wind model uses time series from multiple sky maps, and reduces signals that do not participate in the outward progression of the solar wind, gaps or bad spots in the data are filled in to provide continuous inner-heliospheric coverage. For most of the time period covered by the reconstructed sky maps, the area blanked out near the center of the direct sky maps of Fig. 7 is located in approximately the same place. This region is back-filled somewhat from the lines of sight that exist at larger elongations, and more at some position angles than others to a circle set at 18° from the Sun. Since few non-heliospheric artifacts such as zodiacal light and aurora remain in these maps constructed from volumes from the edited time series, the image contrast of



(a)



(b)

(c)

Fig. 7. Brightness increase of the 27–28 May 2003 ICMEs as they move outward from the Sun. Brightness is in S10 units. (a) Hammer-Aitoff sky map projection that presents the lines of sight used within ± 1.5 hours of the time indicated. The coverage used to provide the 3D reconstructions is approximately the same throughout the Carrington rotation that includes the ICME. (b) and (c) Fisheye sky map presentation at the times indicated showing the ICME outward progression.

the map can be enhanced above that of direct sky maps, thus highlighting more detail.

4. Remote-Observer Views and *in-situ* Comparisons

The 3D-reconstructed volumes can also be viewed as a remote observer would view them or be used to determine a mass within a specific region of the reconstruction volume as in Fig. 8. Perhaps more pertinent are planar cuts through the volumetric data and *in-situ* comparisons. Figure 9 gives one such example for the 27–28 May 2003 ICME sequence in the SMEI data, and also shows the 3D-reconstruction of the associated velocity during this period. Regions that are accessed by fewer than ten lines of sight per resolution element in the SMEI analysis are left blank, and these locations are carried over to the much lower resolution volume elements in the velocity data unless they too have fewer than the required number, at which location they are also left blank. Both 3D-reconstructed velocity and density are combined to determine ram pressure for the ICME highlighted in this example, and are shown as the primary example of these measurements available at Mars and compared with Mars Global Surveyor magnetic field measurements⁹.

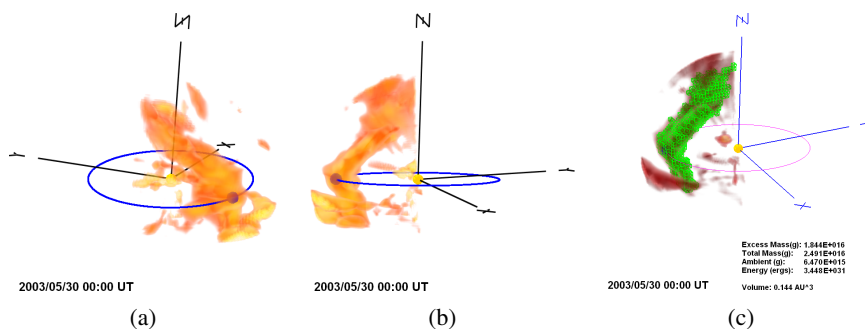


Fig. 8. 3D mass determination for the 27–28 May 2003 halo CME sequence as the associated ICMEs reach Earth vicinity at 00:00 UT 30 May 2003. Electron density is contoured upward from 15 cm^{-3} . (a) The ICME observed from about 45° East of the Sun-Earth line and 20° above the ecliptic plane, just as the event sequence begins to engulf the Earth. (b) The ICME observed from about 70° West of the Sun-Earth line and 5° above the ecliptic plane. (c) The total event now highlighted and filled with cubes from approximately this same perspective, has a volume of 0.144 AU^3 above this contour level, a total mass of $2.49 \times 10^{16} \text{ g}$, and is comprised of several halo CMEs. (see Jackson *et al.*⁷).

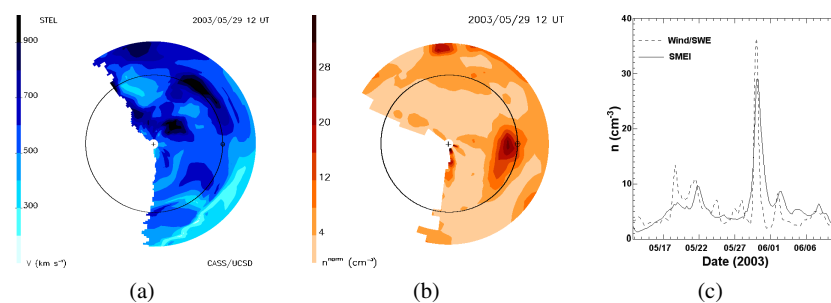


Fig. 9. 3D reconstruction of the 27–28 May 2003 halo ICME sequence of events as it reaches Earth displayed as an ecliptic-plane cut of the reconstruction at the time indicated, as viewed down from the North. The Sun is at the center marked with a +, an ellipse marks the Earth’s orbital path in the ecliptic, and the Earth is shown by \oplus . (a) A velocity cut at the time indicated. There is high velocity to the West of the Sun-Earth line associated with the CME sequence. (b) A density cut at the same time as in (a). The density scale is given to the left. To best display the structure, an r^{-2} density fall-off has been removed to scale densities to 1 AU. The main structure at Earth is associated with the halo CME sequence observed by LASCO on 27–28 May 2003, and shows that the density enhancement of the ICME hitting Earth in this event is more extensive to the East of the Earth than to the West (from Jackson *et al.*⁷). (c) Time-series plot of the density at Earth from the reconstruction and from Wind proton observations for the whole Carrington rotation that includes the ICME. The latter *in situ* observations are combined into 12-hour averages matching the temporal and spatial resolutions of the SMEI reconstruction. The correlation coefficient within 6 days of the ICME passage is 0.86⁷.

5. Conclusions

We have described the mathematical analyses in the current UCSD 3D-reconstruction algorithm, and given examples of some of the recent measurements and presentations that they provide. The time-dependent analysis programs using IPS data from STELab and Thomson-scattering brightness data from SMEI now reside at the CCMC for use by others. This article serves as an explanation for these analyses, and some of the caveats present in using them. The actual Fortran programs used in these analyses that are here described mathematically are available from both the CCMC and the UCSD Website at: <http://cass.ucsd.edu/solar/resources.html#resources>.

Acknowledgments

We thank M. Kojima for his encouragement throughout the length of this project and for originally making available IPS data for these analyses

under the auspices of a joint CASS/UCSD-STELab cooperative agreement. SMEI was designed and constructed by a team of scientists and engineers from the US Air Force Research Laboratory, the University of California at San Diego, Boston College, Boston University, and the University of Birmingham, UK. The authors also wish to thank the Wind/SWE group for use of their data. The work of B.V. Jackson, A. Buffington, P.P. Hick, and J.M. Clover was supported at the University of California at San Diego by NSF grants ATM-0331513 and ATM-0852246 and NASA grants NAG5-134543 and NNG05GG45G. In addition, M.M. Bisi and B.V. Jackson were supported in part by AFOSR grant FA9550-06-1-0107.

References

1. C. J. Eyles, G. M. Simnett, M. P. Cooke, B. V. Jackson, A. Buffington, P. P. Hick, N. R. Waltham, J. M. King, P. A. Anderson and P. E. Holladay, The Solar Mass Ejection Imager (SMEI), *Solar Phys.* **217** (2003) 319.
2. B. V. Jackson, A. Buffington, P. P. Hick, R. C. Altrrock, S. Figueroa, P. Holladay, J. C. Johnston, S. W. Kahler, J. Mozer, S. Price, R. R. Radick, R. Sagalyn, D. Sinclair, G. M. Simnett, C. J. Eyles, M. P. Cooke, S. J. Tappin, T. Kuchar, D. Mizumo, D. F. Webb, P. Anderson, S. L. Keil, R. Gold and N. R. Waltham, The Solar Mass Ejection Imager (SMEI) mission, *Solar Phys.* **225** (2004) 177.
3. A. Buffington, J. S. Morrill, P. P. Hick, R. A. Howard, B. V. Jackson and D. F. Webb, Analyses of the comparative responses of SMEI and LASCO, *Proc. SPIE* **6689** 66890B (2007) 1–6, doi:10.1117/12.734658.
4. B. V. Jackson, A. Buffington, P. P. Hick, X. Wang and D. Webb, Preliminary three-dimensional analysis of the heliospheric response to the 28 October 2003 CME using SMEI white-light observations, *J. Geophys. Res.* **111**(A4) (2006) A04S91.
5. B. V. Jackson, P. P. Hick, A. Buffington, M. M. Bisi, M. Kojima, and M. Tokumaru, Comparison of the extent and mass of CME events in the interplanetary medium using IPS and SMEI Thomson scattering observations, in *Astronomical and Astrophysical Transactions* edited by I. Chashei and V. Shishov, **26**(6) (2007) 477–487, doi:10.1080/10556790701612221.
6. M. Kojima and T. Kakinuma, Solar-cycle evolution of solar-wind speed structure between 1973 and 1985 observed with the interplanetary scintillation method, *J. Geophys. Res.* **92** (1987) 7269.
7. B. V. Jackson, M. M. Bisi, P. P. Hick, A. Buffington, J. M. Clover and W. Sun, Solar Mass Ejection Imager (SMEI) 3D reconstruction of the 27-28 May 2003 CME sequence, *J. Geophys. Res.* **113** A00A15 (2008) doi:10.1029/2008JA013224.

8. M. Tokumaru, M. Kojima, K. Fujiki, M. Yamashita and B. V. Jackson, The source and propagation of the interplanetary disturbance associated with the full-halo coronal mass ejection on 2003 October 28, *J. Geophys. Res.* **112** A05106 (2007) doi:10.1029/2006JA012043.
9. B. V. Jackson, J. A. Boyer, P. P. Hick, A. Buffington, M. M. Bisi and D. H. Crider, Analysis of solar wind events using interplanetary scintillation (IPS) remote sensing 3D reconstructions and their comparison at Mars, *Solar Phys.* **241** (2007) 385.
10. G. E. Brueckner, R. A. Howard, M. J. Koomen, C. M. Korendyke, D. J. Michels, J. D. Moses, D. G. Socker, K. P. Dere, P. L. Lamy, A. Llebaria, M. V. Bout, R. Schwenn, G. M. Simnett, D. K. Bedford and C. J. Eyles, The Large Angle Spectroscopic Coronagraph (LASCO): visible light coronal imaging and spectroscopy, *Solar Phys.* **162** (1995) 357.
11. M. L. Kaiser, The STEREO mission: an overview, *Adv. Space Res.* **36** (2005) 1483.
12. B. V. Jackson, P. L. Hick, M. Kojima and A. Yokobe, Heliospheric tomography using interplanetary scintillation observations, 1. Combined Nagoya and Cambridge observations, *J. Geophys. Res.* **103** (1998) 12049.
13. K. Asai, M. Kojima, M. Tokumaru, A. Yokobe, B. V. Jackson, P. L. Hick and P. K. Manoharan, Heliospheric tomography using interplanetary scintillation observations, 3. Correlation between speed and electron density fluctuations in the solar wind, *J. Geophys. Res.* **103** (1998) 1991.
14. M. Kojima, M. Tokumaru, H. Watanabe, A. Yokobe, K. Asai, B. V. Jackson and P. L. Hick, Heliospheric tomography using interplanetary scintillation observations, 2. Latitude and heliocentric distance dependence of solar wind structure at 0.1-1 AU, *J. Geophys. Res.* **103** (1998) 1981.
15. P. P. Hick and B. V. Jackson, Heliospheric tomography: an algorithm for the reconstruction of the 3D solar wind from remote sensing observations, *Proc. SPIE* **5171** (2004) 287–297.
16. B. V. Jackson, A. Buffington and P. P. Hick, A heliospheric imager for Solar Orbiter, in *Proc. of Solar Encounter: The First Solar Orbiter Workshop*, Puerto de la Cruz, Tenerife, Spain, 14–18 May 2001 (*ESA SP*) **493** (2001) 251.
17. M. M. Bisi, B. V. Jackson, P. P. Hick, A. Buffington and J. M. Clover, 3D reconstructions of the early November 2004 CDAW geomagnetic storms: preliminary analysis of STELab IPS speed and SMEI density, *J. Geophys. Res. — Space Physics Special Edition — Geomagnetic Storms of Solar Cycle 23* **113** (2008) A00A11.
18. B. V. Jackson and P. P. Hick, Corotational tomography of heliospheric features using global Thomson scattering data, *Solar Phys.* **211** (2002) 344.
19. A. T. Young, Interpretation of interplanetary scintillation, *Astrophys. J.* **168** (1971) 543.
20. B. V. Jackson, P. P. Hick, A. Buffington, M. Kojima, M. Tokumaru, K. Fujiki, T. Ohmi and M. Yamashita, Time-dependent tomography of heliospheric features using interplanetary scintillation (IPS) remote sensing observations, *Solar Wind 10 Conference Proceedings*, Pisa, June 17–21 (2002), pp. 31–34.

21. D. E. Billings, A guide to the solar corona, Academic, New York, (1966) 150.
22. S. J. Tappin, A. Buffington, M. P. Cooke, C. J. Eyles, P. P. Hick, P. E. Holladay, B. V. Jackson, J. C. Johnston, T. Kuchar, D. Mizuno, J. B. Mozer, S. Price, R. R. Radick, G. M. Simnett, D. Sinclair, N. R. Waltham and D. F. Webb, Tracking a major interplanetary disturbance with SMEI, *Geophys. Res. Lett.* **31** (2004) L02802.